

Non Linear Phase model for correction of magnetic field inhomogeneity Effects in Quantitative gradient Echo based MRI

Author : C.Fatnassi^{1,2}, G.Krueger^{2,3}, R.Meuli³ and K.O'Brien^{2,4} ,
chemseddine.fatnassi@unil.ch

1 Université de Lausanne/Centre Hospitalier Universitaire de Lausanne, Lausanne, Switzerland, 2 CIBM - AIT, école Polytechnique Fédérale de Lausanne, Lausanne, Switzerland, 3 Advanced Clinical Imaging Technology, Siemens Healthcare IM BM PI, Lausanne, Switzerland, 4 Hopitaux Universitaires de Genève, Genève, Switzerland
1^{er} mars 2014

Abstract

$R2^*$ plays an important role in the quantitative evaluation of the brain function and tissue iron content. Unfortunately, susceptibility induced macroscopic field inhomogeneities B_{0macro} across an image voxel act to increase the $R2^*$ in a gradient echo image. If these B_{0macro} are measurable [17] their influence can be removed in post processing. Conventionally, these algorithms assume the phase evolves linearly with time; however, in the presence of a large B_{0macro} , e.g. near the edge of the brain, this assumption is broken [27]. The phase evolution appears random. In this work, we hypothesize that the phase evolution in the presence of large B_{0macro} , can be modeled and corrected using 1D-random-walk theory.

MRI ; gradient echo ; EPI ; magnetic susceptibility ; magnetic field inhomogeneities

1 Introduction

Quantitative magnetic resonance (MR) imaging by means of $T2^*$ relaxometry is becoming an increasingly requested tool in many areas of MR imaging. The effective transverse relaxation rate $R2^*(1/T2^*)$ characterizes static magnetic field variation on the macroscopic and mesoscopic level[4], which is quantitatively associated with local concentrations of paramagnetic macromolecules that can reveal the physiology of disordered brain function [20]. It is applied for BOLD contrast studies[23, 14] as well as for the assessment of iron content in the brain [6], heart [5], and liver [22], dynamic susceptibility contrast MRI [2, 18], cerebral venous blood volume measurement [9] and brain abnormalities detection like MS (Multiple Sclerosis) [16]. However it is well known that the presence of the macroscopic field inhomogeneities B_{0macro} increases the intravoxel dephasing in gradient echo (GRE) MR imaging. This leads to an apparent increase in the signal decay

resulting in regions of no or low signal. In quantitative GRE MR imaging, the presence of the B_{0macro} leads to inaccurate $R2^*$ quantification, consequently an erroneous diagnostic and interpretation of the fast signal decay may occur. Over the past few years, numerous preprocessing and post-processing methods have been proposed to correct for the susceptibility induced B_{0macro} intravoxel dephasing. Preprocessing techniques aim to manipulate the slice selection gradient [13] or radiofrequency pulses which is based on field gradient compensation technique [19]. Post-processing techniques aim to remove the influence of the B_{0macro} by measuring or estimating the extent of intravoxel dephasing. For 2D GRE imaging, Fernandez-seara and Wehrli [17] proposed an iterative postprocessing technique to correct from the Sinc modulation generated by a linear gradient in the slice direction. Their method was later optimized by Dahnke et al [10]. Huairan Zeng et al [27] introduced a Point Spread Function (PSF) method to correct the EPI image distortion ; however, this technique needs an additional phase encoding acquisition. More complex signal behavior generated by nonlinear macroscopic B_{0macro} inhomogeneities has been investigated by Xiangyu Yang et al [25]. They derived an analytical solution to correct for a quadratic gradient through the slice ; it was shown to be of particular importance for low resolution imaging (slice thickness greater than the inplane resolution). Diego Hernando et al [3] introduced a method to correct from the macroscopic field inhomogeneities in the presence of fat ; they used a third-order polynomial to model the field variations and the modulation term is calculated numerically. Lastly, Yablonskiy et al [26] introduced the Voxel spread function (VSF), based on a linear gradient evolution across the voxel to correct for the magnetic field inhomogeneity in quantitative GRE imaging. The basic theory has recently been extended to 3D [4]. In region with high SNR and low susceptibility like the center of the brain ; the mentioned algorithms remove successfully the field inhomogeneities variation artifacts from the $R2^*$ maps ; but in region with low SNR and high susceptibility artifact like near the paranasal sinus, most of the algorithms fail. This could be caused by two most important issues : the choice of the field variation model across the image voxel and the phase evolution as function of echo times. Concerning the first problem, the ideal combination of the polynomial fit order and the number of the voxel neighbors reduces the fitting noise and consequently increases the accuracy of the correction ; some previous studies show that choice of voxel neighbors and fit order are strongly depending on image resolution. Thus increasing blindly these parameters may lead to noise fitting rather than increasing accuracy. Regarding the phase evolution, all of these methods assume that the phase evolves linearly as function of time. However in 2005, Huair.Zeng et al [27] demonstrated by simulation and from invivo DATA that the linear assumption is broken in the presence of a large field gradient, which is in agreement with what we have observed with 3T data, where the effect of susceptibility induces B_{0macro} is expected to be worse. To the best of our knowledge no model currently tries account for non-linearity of the phases evolution with time. We hypothesize that the overcorrection observed e.g in the paranasal sinus, is due to the linear phase evolution assumption being broken. Herein we propose an analytical solution for the phase dispersion over the echo time based on the principles of 1D random walk theory [15, 21]. This approach called Non Linear Sinc Correction combines the linear gradient behavior across an image voxel and the probabilistic phase behavior as

function of echo time. The new method is validated with simulations and tested on phantom and invivo DATA, then compared with the non-iterative 3D Linear Sinc Correction LSC described in [17, 10].

2 Theory

In the following section we will briefly review the fundamental steps to linear correction models [ref] which assume a linear evolution of phase with time. For a more complete description we refer the reader to [4]. The theory will then be expanded to consider a non-linear phase evolution with time, introduce a new method to calculate the field map and Linear phase evolution. The MR signal in a 3D gradient echo experiment for given n th voxel acquired in the presence of inhomogeneous magnetic field $\Delta B_n(r)$ which is assumed equivalent through all vector position directions r can be written as :

$$S_n(K; TE_N) = \gamma \int_{-\infty}^{\infty} dr \rho_n(r; TE_N) e^{-i2\pi K r} F_n(r; TE_N) \quad (1)$$

Where $\rho_n(r; TE_N)$ is the ideal signal decay in the absence of the field inhomogeneities,

$$F(r; TE_N) = e^{-i\Delta\phi(r; TE_N)} \quad (2)$$

eq.2 describes the signal loss due to the macroscopic $\Delta B_n(r)$ inhomogeneities. And the k-space is defined conventionally as :

$$2\pi k_x = \gamma G_x t_x; 2\pi k_y = \gamma G_y t_y; 2\pi k_z = \gamma G_z t_z \quad (3)$$

where G_x, G_y are the phase encoding and G_z the read-out, $t_{x,y,z}$ are the duration of the gradients. Assuming a linear phase evolution as function of time, the phase shift $\Delta\phi_n$ can be described by λ^{th} order function across an image voxel as follow :

$$\Delta\phi_n(TE_N) = \gamma \Delta TE_N \sum_{k=0}^{\lambda} a_{\lambda-k} r^{\lambda-k} \quad (4)$$

Where a is the field map fit coefficients, n is the fit order and r is the 3D spatial resolution X, Y and Z . TE_N is the echo time difference between the N^{th} echo and the first echo. In the case where the echo time spacing is fixed, we substitute ΔTE_N by $N\Delta TE$, where ΔTE is the echo time spacing. The MR signal can then be rewritten as follows :

$$S_n(k; TE_N) = \int_{-\infty}^{\infty} dr \rho_n(r; TE_N) e^{-i2\pi k r + i\gamma N TE_1 \sum_{j=0}^{\lambda} a_{\lambda-j} r^{\lambda-j}}$$

2.1 Nonlinear phase evolution

To extend the model further let us consider that the phase evolution can be described as combination of a linear $\Delta\phi_n(T E_N)$ and an error component ϵ :

$$\phi_n(T E_N) = \phi_{0n}(T E_N) + \Delta\phi_n(T E_N) + \epsilon_n(T E_N) \quad (6)$$

When the B_{0macro} inhomogeneities are small then the linear term, $\Delta\phi_n(T E_N) \gg \epsilon_n(T E_N)$, dominates the phase evolution and $F_n(r; T E_N)$ is well approximated using a linear relationship [5, 22]. However as the B_{0macro} inhomogeneities become larger the linear term no longer dominates the phase evolution $\Delta\phi_n(T E_N) \simeq \epsilon_n(T E_N)$. The linear relationship no longer holds [27] and the evolution appears non-linear, until eventually the error term dominates $\Delta\phi_n(T E_N) \ll \epsilon_n(T E_N)$ and the phase evolution appears like noise.

If instead of the conventional assumption of phase evolving linearly with time we consider that the phase evolves using the principles of Gaussian Random walk theory we can generate a model to describe the intravoxel dephasing based on the expected variance of the phase dispersion $\sigma_n(T E_N)$. The expected variance of the phase dispersion can be described as follows :

$$\sigma_n(T E_N)^2 = \langle \phi_n(T E_N)^2 \rangle = \sum_{i=1}^N \sum_{j=1}^N \langle \omega_i \cdot \omega_j \rangle \delta\phi_n(\Delta T E)^2 \quad (7)$$

Where $\omega_{i,j}$ determines the phase variations in time relative to the mean phase value $\langle \phi_n(T E_N)^2 \rangle$, $\delta\phi$ is the mean phase step over time and $i, j = 1, 2, 3 \dots N$ is the echo number. $\Delta T E$ denotes the echo time spacing. To simplify further the theory, the coefficients $\omega_{i,j}$ are defined as :

$$\langle \omega_i \cdot \omega_j \rangle = \begin{cases} 0 & i \neq j \\ \beta_n & i = j \end{cases} \quad \text{thus} \sum_{i=1}^N \sum_{j=1}^N \langle \omega_i \cdot \omega_j \rangle = N \cdot \beta_n \quad (8)$$

Finally we can describe the phase shift over the echo time in the presence of large $\Delta B(r)$ inhomogeneities as function of the echo number and β_n as follows :

$$\phi_n(T E_N) - \phi_n(T E_1) = \epsilon_n(T E_n) = (N \cdot \beta_n)^{1/2} \delta\phi_n(\Delta T E) \quad (9)$$

The coefficient β can be described using different approaches. In 1D random walk theory, β calculation is based on the values that $\omega_{i,j}$ can take. Conventionally $\omega_{i,j} \in [-1, 1]$, consequently β will tend to 1. But from our simulation, phantom and in-vivo DATA, the phase variations over the echo time are larger and consequently $\omega_{i,j}$ interval can become wider. Therefore $\omega_{i,j}$ coefficients are defined as :

$$\begin{cases} \omega_i = [-\alpha; \alpha] & \text{and } \alpha = \text{abs}[\frac{\text{Max}(\phi_n(T E_N))}{\phi_n(T E_1)}] \\ \omega_j = \omega_i \end{cases} \quad \text{thus } \beta_n = \langle [-\alpha; \dots; \alpha]^2 \rangle \quad (10)$$

2.2 Signal correction

The MR image signal can be computed as the IFT (inverse Fourier Transform) of the signal $S_n(TE_N)$:

$$S_n(TE_N) = \frac{1}{V_n k} \int_k \int_r S_n(K; TE_N) \cdot e^{-i2\pi kr} dk ; k_{x,y,z} = \frac{2\pi}{\gamma G_{x,y,z}} \quad (11)$$

where L is the voxel dimension, $V_n = L_x L_y L_z$ is the voxel volume. In order to obtain the analytical IFT expression of the k-space signal, we use some approximations which are valid in high MR image resolution. The first approximation considers that the signal is described by rectangular function across the voxel dimensions which limit the integral in eq.1 :

$$S_n(TE_N) = \frac{1}{V_n} \int_{-\frac{L_r}{2}}^{\frac{L_r}{2}} dr \rho_n(r; TE_N) \cdot e^{-i2\pi kr} \cdot F_n(r; TE_N) \quad (12)$$

where L_r is the image spatial resolutions. The signal IFT of the signal $S_n(K; TE_N)$ after the mentioned approximation can be written as :

$$S_n(TE_N) = \frac{1}{V_n} \rho_n(r; TE_N) \int_{-\frac{L_r}{2}}^{\frac{L_r}{2}} dr \cdot e^{-i(N \cdot \beta_n)^{1/2} \delta \phi_n(\Delta TE)} \quad (13)$$

So :

$$S_n(TE_N) = \frac{1}{V_n} \rho_n(r; TE_N) \int_{-\frac{L_r}{2}}^{\frac{L_r}{2}} dr \cdot e^{-i\gamma(N \cdot \beta_n)^{1/2} \Delta TE_N \sum_{j=0}^{\lambda} a_{\lambda-j} r^{\lambda-j}} \quad (14)$$

The second approximation considers that the distribution of the field inhomogeneities evolves slowly through the image voxel; therefore the field gradient which is in our approach the coefficient $a_{\lambda-k}$ in eq.3 can be computed from the field map, setting $\lambda = 1$ (first order fit) and using the central difference approximation as follows :

$$a_{n,r} = \frac{(\Delta B_{n+1,r} - \Delta B_{n-1,r})}{2L_r} \quad (15)$$

Therefore the MR signal with the linear approximation of the field gradient across the voxel can be described as :

$$S_n(TE_N) = \frac{1}{V_n} \rho_n(r; TE_N) \prod_r L_r \text{sinc}\left(\frac{\gamma}{2}(N \cdot \beta_n)^{\frac{1}{2}} \Delta TE a_{1,n,r} L_r\right) \quad (16)$$

To limit the noisy phase effect which becomes large when the echo time tends to increase, also the field gradient over estimation in regions with low signal to noise ratio e.g. paranasal

sinus region and near the brain edges, which lead to artificial over correction, we introduce a normalized weighting factor $\psi(TE_N)$ (similar to the field map weighting factor) that limit the correction of the signal decay as follows :

$$\psi(TE_N) = \frac{S_n(TE_N) - S_n(TE_1)}{S_n(TE_N)} \quad (17)$$

where

$$\begin{cases} \psi(TE_N) \rightarrow 1 & \text{artificial signal decay} \\ \psi(TE_N) \rightarrow 0 & \text{normal signal decay} \end{cases} \quad (18)$$

An additional complication arises because the macroscopic field gradient $\Delta B_n(r)$ can cause voxel dimensions distortion (unless the imaging gradient $G(x, y, z)$ is much stronger) [23, 14]. In this case, the voxel dimensions need to be modified, since the true voxel dimensions are no longer L_r , but $\lambda_n L_r$ [5, 13], where :

$$\lambda_n = \frac{G_r}{G_r + \Delta B_n(r)} \quad (19)$$

Finally, we can describe the MR signal decay modulated with the 3D sinc function using the random walk theory to calculate the analytical phase dispersions over the echo time as :

$$S_n(TE_N) = \frac{1}{V_n} \rho_n(TE_N) \prod_r L_r \text{sinc}\left(\frac{\gamma}{2} \psi(TE_N) (N \cdot \beta_n)^{\frac{1}{2}} \Delta TE \ a_{1,n,r} L_r\right) \quad (20)$$

To solve this equation and correct from the signal decay caused by the 3D sinc function modulation and nonlinear phase evolution as function of echo time, we determine from the DATA the sinc function parameters and we divide the image signal by the proposed analytical modulation. We should keep in mind that this approach doesnt take in consideration the signal phase shift at $TE = 0$, resulting from the RF field inhomogeneities which is negligible and not essential for correction.

2.3 Weighted Field Map Computation

Conventionally, the phase DATA is fitted linearly and the field map is calculated by the slope of the fit. Herein, we propose a new approach to compute the field map. The field map of nth voxel is represented by the phase step $\delta\phi_n(\Delta TE)$, in other words the field map is computed as the mean standard deviation of the unwrapped phase signal over the echo times and weighted by the signal intensity ratio W_n where :

$$W_n = \frac{S_n(TE_N)}{\sum_{i=1}^N S_n(TE_N)} \quad (21)$$

and

$$\Delta B_n = \frac{1}{N \Delta TE} \delta\phi(\Delta TE) = \sum_{i=1}^N \frac{1}{2\pi N \Delta TE} (\phi_{n,TE_1} - \phi_{n,TE_N} \cdot W_n) \quad (22)$$

where n is the voxel coordinates and N is the echo number, $S_n(TE_N)$ is the signal intensity of the magnitude DATA in the imaging domain. Median and Gaussian filter were applied on the weighted field map [9] to reduce the noise in regions with low SNR and remove some phase coil combinations artifacts. Because the field map values are weighted by the signal intensity ratio W_n at the corresponding location, the field estimation is robust especially in region with low SNR [12]

3 Methods

3.1 Numerical Phantom

To test our hypothesis and methods we developed a numerical phantom, using customized Matlab scripts (Mathworks, USA), to simulate the effect of B_{0macro} , Fig.1. First, the data set used in this simulation is provided by McConnell Brain Imaging Centre, Montreal Neurological Institute. It consists of anatomical images segmented into disjoined special masks or templates (one per tissue type). The MR brain properties : $T1$ $T2^*$ PD (grey matter, white matter, csf,) were set to mimic our real brain DATA and used to simulate the magnitude signal of multi gradient echo sequence using an analytical solution to the Bloch equation :

$$S_n(TE_N) = \frac{M_{n,0} e^{\frac{-TE_N}{T_2^*}} \sin(\alpha) (1 - e^{\frac{-TR}{T_1}})}{1 - \cos(\alpha) e^{\frac{-TR}{T_1}}} \quad (23)$$

where $M_{n,0}$ is the ideal signal free from the field gradient inhomogeneties and α is the flip angle. To evaluate the B_{0macro} effects in more detail and in a wider range than the experimental condition ; a total of 40 echoes were simulated using the following sequence parameters $TR/TE1/\Delta TE = 47/1.23/1.23ms$, flip angle 10 and $1mm^2$ inplane resolution to limit the field variation across the pixel to a linear behavior. Different degrees of B_{0macro} were introduced by taking a typical field map from an invivo experiment on 3.0 T scanner and scaling it to range between 1-80Hz/cm. Corrupted magnitude data was subsequently calculated using equation 20 multiplied by the function $F_n(r; TE_N)$ which describes the signal loss due to the macroscopic B_{0macro} . The phase images were then simulated according to equation 5 using the first phase image of the invivo field map and modeling the error term as random noise which depends on the simulated magnitude image. The weighted field map was computed from the simulated phase images according to eq.11 and the 3D LS and 3D NLS corrections were performed on the corrupted magnitude images and compared to the true $R2^*$ values used.

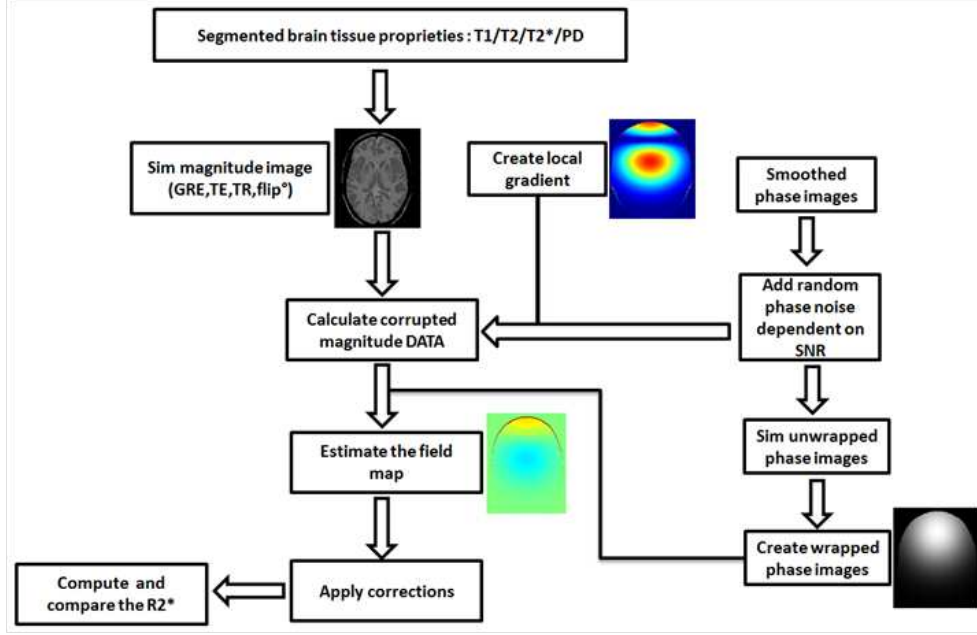


FIGURE 1: GRE DATA Simulation and correction using LSC and NLSC.

3.2 MRI acquisition

All scans were performed on a 3T (Magnetom Trio, Siemens AG, Healthcare Sector, Erlangen, Germany) using 32-channel phased-array coil. Phantom and in-vivo data were acquired with a 3D bi-polar multi gradient echo sequence. 32 echoes were acquired with $TR/TE1/ = 47/1.23/1.23ms$, flip angle 8, $1.6mm^3$ isotropic resolution and a matrix size of $36 \times 136 \times 112$, Grappa parallel imaging with acceleration factor of 2 and an asymmetric echo, and phase partial Fourier sampling factor of 6/8. The weighted field map was computed from the phase and feed as input into the 3D LS and 3D NLS corrections of the magnitude images. The performance of the correction algorithms were evaluated with a cylindrical phantom containing 5 spheres filled with water doped with $MnCl_2 - 4H_2O$ with the following concentrations 10-20-40-70-120 mg per lL of distilled water in order to examine the linearity of the $R2^*$ value as function of the manganese concentration [7]. To assess the accuracy of our method, the GRE images from simulation, phantom and in-vivo experiments were corrected using our algorithm which is based on the random walk theory to describe the non-linearity of the phase evolution as function of echo time and the non-iterative version of a post processing technique, which is based on linear phase evolution assumption described in [17, 10]. To obtain an equivalent comparison, we also introduced the weighting factor $\psi(TE_N)$ in the second algorithm. In order compute the $R2^*$ maps, we introduce a new method similar to the numerical trapezoidal integration described in [11], but instead using Simpson rule. Thus the $R2^*$ maps were computed from both corrected

and non-corrected magnitude DATA as follows :

$$R_{2,n}^* = \frac{S_n(TE_1) - S_n(TE_N)}{\frac{1}{6}(TE_N - TE_1)[S_n(TE_1) + S_n(TE_N) + 4S_n(\frac{TE_1+TE_N}{2})]} \quad (24)$$

To further evaluate our approach in correcting the field inhomogeneities on real DATA, we chose 14 in vivo DATA which suffer from big signal loss in the paranasal sinus region and especially in grey-matter/air interfaces, and then we corrected the DATA using LSC and NLSC ; Fig.8 presents a Boxplot of $R2^*$ values for the selected 14 in-vivo DATA. VOI drawn in the paranasal sinus region where the field gradient is large ($> 50Hz/cm$) after correction with LSC and NLSC and compared with the $R2^*$ values of VOI drawn in the center of the brain where the field inhomogeneities are small (artifact free or Ideal $R2^*$). As mentioned in the introduction, the macroscopic field inhomogeneities correction can be used in different applications. Herein we investigated the effect of the field inhomogeneities correction on the detection of iron deposit. It is well known that the iron deposition (Hemosiderin) can lead to field distortion around the lesion (Blooming artifact), consequently the bleeding area appears larger [8]. For this, we use a patient DATA containing a lesion with iron deposit in the brain ; we overlap the non-corrected and corrected $R2^*$ map with both NLSC and LSC on the MP2rage image, then compare the size of the iron deposit lesion, the results are shown in fig.9 and fig.10.

4 Results

4.1 Simulation

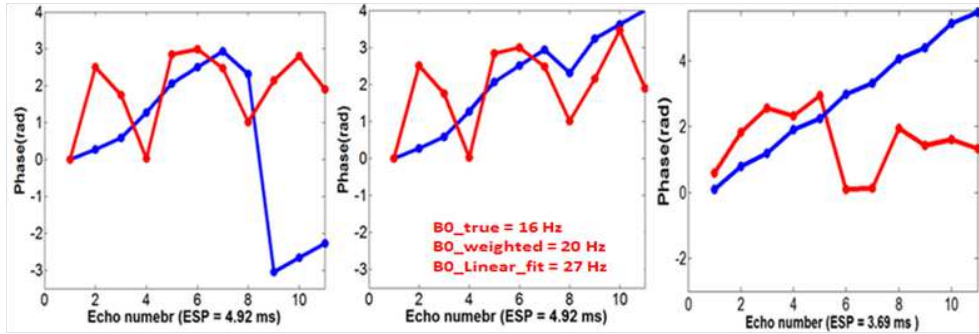


FIGURE 2: Phase behavior as function of time in the presence of low (blue) and high (red) field inhomogeneties. Left and middle image : simulated phase before and after phase unwrapping. Right image : unwrapped phase from phantom DATA.

The simulation results in Fig. 2 illustrate the difficulties in estimating the field map in the presence of B_{0macro} induced intravoxel dephasing. With small field gradient inhomogenei-

ties the phase can be reliably unwrapped and a linear regression can be used to effectively estimate the underlying field inhomogeneity ; however, in cases where the field inhomogeneity is large unwrapping the data may not be possible as the noise may mask the phase jumps. The field map value of the phase in presence of high field inhomogeneties (Fig. 2 middle image) was calculated using the linear fit, the weighted sum method and compared with the true value introduced in simulation and the results are shown on the Fig. 2. In this scenario the proposed weighted field map reduces the error by 40% .In addition ; the phase behaves linearly in the presence of low field gradient (blue line), but as soon as the field gradient increases, the linearity is lost. Fig. 3 represents the simulated inverse $F_n(r; TE_N)$ in the presence of small (circle) and large (triangle) field gradient, using the LSC (blue line) and the NLSC (red line). This simulation allows to us the observation of the correction coefficient ($1/F(t)$) behave which we use while correcting our magnitude signal. In the presence of small field gradient (circle). Fig. 4 represents the simulated 2D-GRE DATA .Upper row : the $R2^*$ maps ; left image : corrupted $R2^*$, middle and right images show $R2^*$ maps corrected with LSC and NLSC respectively. Middle row : Computed relative difference to the non-corrupted $R2^*$ map in order to evaluate the quantitative metric changes. Lower row : the Structural SIMilarity index (SSIM) is calculated between the three $R2^*$ maps and the original one to assess the visual quality metric [24].

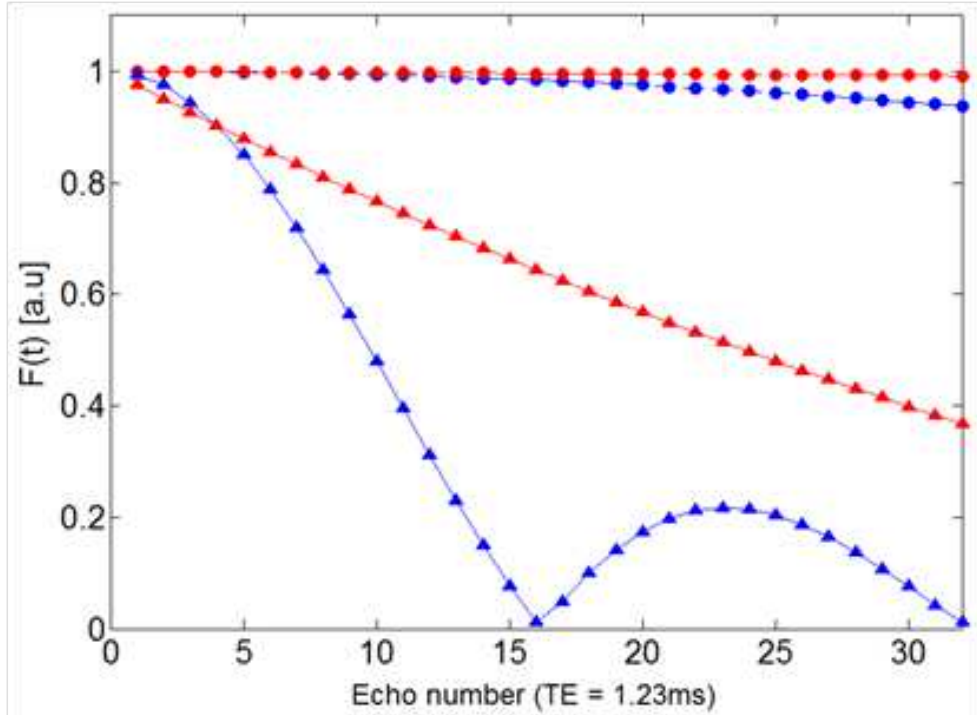


FIGURE 3: Simulated inverse $F_n(r; TE_N)$ in the presence of small (circle) and large (triangle) field gradient, using the LSC (blue line) and the NLSC (red line).

4.2 Phantom

Results of phantom study are presented in Fig. 5. As described in method section, the phantom consisted of cylinder containing 5 spheres filled with different concentration of $MnCl_2 - 4H_2O$. The phantom was oriented parallel to the main magnetic field B_0 . The presence of air bubble inside the spheres and near the phantom edges creates strong magnetic field inhomogeneities and leads to signal drop over time and Consequently $R2^*$ overestimation. In Fig. 6, we demonstrate the accuracy of the tow correction methods where the $R2^*$ values are plotted against the $MnCl_2 - 4H_2O$ concentrations. As known from literatures, $R2^*$ values increase linearly with the increasing $MnCl_2 - 4H_2O$ concentration within the phantom spheres [7]; this linear relationship allows us to assess the performance of our algorithm on real DATA.

4.3 Invivo

Results of in-vivo DATA obtained from a human subject were presented in Fig. 7. Left image presents the $R2^*$ map without any corrections from the macroscopic field inhomogeneity in which we can clearly observe the $R2^*$ overestimation in the paranasal sinus region where the field gradient is high and also near the brain edges; middle and right image images show the $R2^*$ maps corrected with LSC and NLSC respectively. Fig. 8 presents a Boxplot of $R2^*$ values for 14 in-vivo DATA. VOI drawn in the paranasal sinus region where the field gradient is large ($> 50Hz/cm$) after correction with LSC and NLSC and compared with the $R2^*$ values of VOI drawn in the center of the brain where the field inhomogeneities are small (artifact free or Ideal $R2^*$). Figure 9 shows the MP2rage of MS (Multiple Sclerosis) patient with iron deposit lesion which appears as a hyperintensity surrounded by a hypointense signal (left image). Upper row presents a GRE images in different echo times showing the increasing blooming artifact around the iron deposit lesion (red arrows). Lower row shows the overlapped lesion mask which delineated manually from the non-corrected and corrected $R2^*$ maps with LSC and NLSC. The figures show that in the absence of correction, the lesion size can be overestimated by including the blooming artifact while delineating the lesions. Although, after correction with LSC and NLSC, the lesion size the blooming artifact is partially or totally removed and the measured size matches with the that in MP2rage.

5 Discussion

5.1 Nonlinear phase evolution as function of echo time

As shown in Fig. 2, in the presence of large macroscopic field gradient ($> 15Hz/cm$), the linear assumption of the phase evolution as function of echo offsets is broken. The

phase behavior becomes masked by noise which interferes with the temporal unwrapping. The phantom DATA also shows the same phase behavior in the presence of low and high field gradient inhomogeneities. These results are in agreement with those found in [2]. In this case it is difficult to expect the true phase dispersion across the time if we use the linear phase evolution assumption and thus, a signal over estimation correction may occur. The nonlinear phase behavior model is also an issue to consider ; because of the nonlinear phase evolution, no polynomial model can be used to fit the phase in time and measure the phase dispersion except the random walk model. In Fig. 3 , we can observe the correction coefficient ($1/F(t)$) that we use while correcting our magnitude signal. In the presence of small field gradient (circle), both the LSC (blue line) and the NLSC (red line) provide approximately the same solution, that means in region with high signal to noise ratio like the center of phantom or brain and far from the edges, the $R2^*$ map correction is small and can be achieved by the two methods ; on the other hand, we can conclude that no benefits from correcting in such region and any applied correction may introduce an additional error. On the other side, when the field gradient is large (triangle), the correction coefficient drops abruptly when using the LSC showing a large Sinc modulation, which in reality doesnt appears on the magnitude signal decay ; Consequently the signal correction is over-estimated and the $R2^*$ values are under-estimated. The correction coefficient computed using the NLSC represents a moderated and uniform exponential decay which reflecting the true artificial signal drop seen in the GRE DATA.

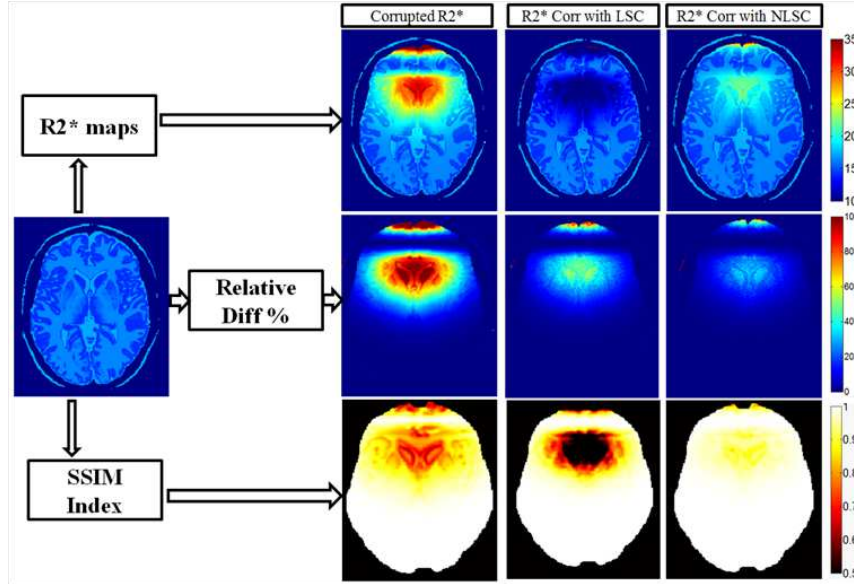


FIGURE 4: Simulation results of $R2^*$ maps correction with LSC and NLSC .Upper row : left image shows the original $R2^*[Hz]$ map without correction ; Middle image shows $R2^*$ map after LSC correction and right image shows the $R2^*$ map corrected with the NLSC. Middle row : images represent the respective relative difference (%). Lower row : the Structural Similarity index (SSIM) maps.

Fig. 4 demonstrate the main features of the proposed Non Linear Sinc correction based on the random walk theory. The corrupted $R2^*$ map mimics the real in-vivo DATA distortion and signal loss mainly in the paranasal sinus region , around the cingulate and near the temporal lobe ; Without correcting the images from the gradient field inhomogeneities, the $R2^*$ is over-estimated ($R2^* = 1/T2^*$) by more than 100% and the biological information and brain structures are lost. In the center of the brain where the field gradient is less than 10Hz/cm, both LSC and NLSC provide approximately the same correction ; although in the presence of large field inhomogeneities, LSC over-estimates the correction and thus under-estimates the $R2^*$ values ; NLSC appears more robust and provide accurate correction, the $R2^*$ values are corrected with an accuracy of 4Hz and the brain structures are well recovered . The computed SSIM when correcting the $R2^*$ map with the LSC remains under 0.7 in region with a large B_{0macro} , but the index increase and becomes high [0.95-1] when the NLSC is applied. This result leads to the conclusion that, in addition to the quantitative $R2^*$ parameter recovery, the NLSC correction also recovers the visual quality of the image structure with reducing noise which affects the qualitative aspect.

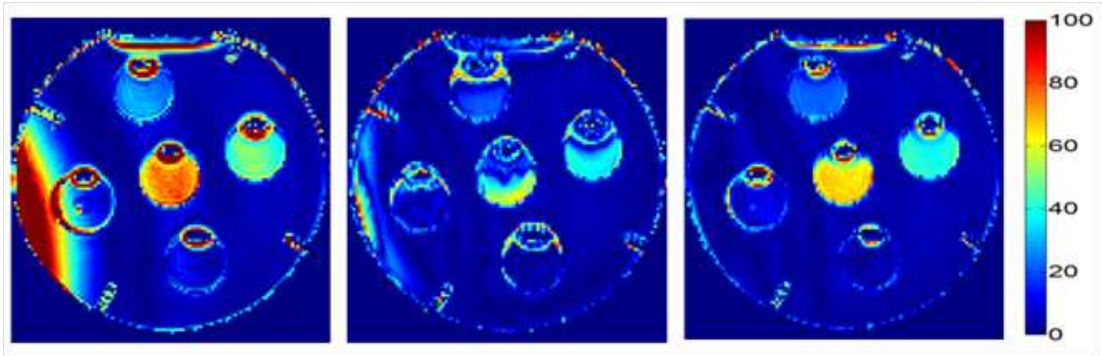


FIGURE 5: Left : Phantom $R2^*$ map [Hz] without correction, middle and right with LSC and NLSC correction respectively. .

As we see in the Fig. 5, the $R2^*$ values are over-estimated near the phantom edges and around the air bubbles, also, a big gradient artifact in right side of the phantom is observed even if a gradient shim was set . The LSC correction reduce the field inhomogeneities artifacts in region with high SNR ; but around the air bubbles, the correction leads to over-estimate the $R2^*$ values, the phantom side artifact and near the edges $R2^*$ over-estimation are partially removed but keeping a high level of noise. NLSC provide more robust correction throughout the phantom whatever the severity of the field gradient inhomogeneities. The $R2^*$ over-estimation within the spheres, near the phantom edges and also the artifact in the left side of the phantom are totally removed with decreasing in local noise.

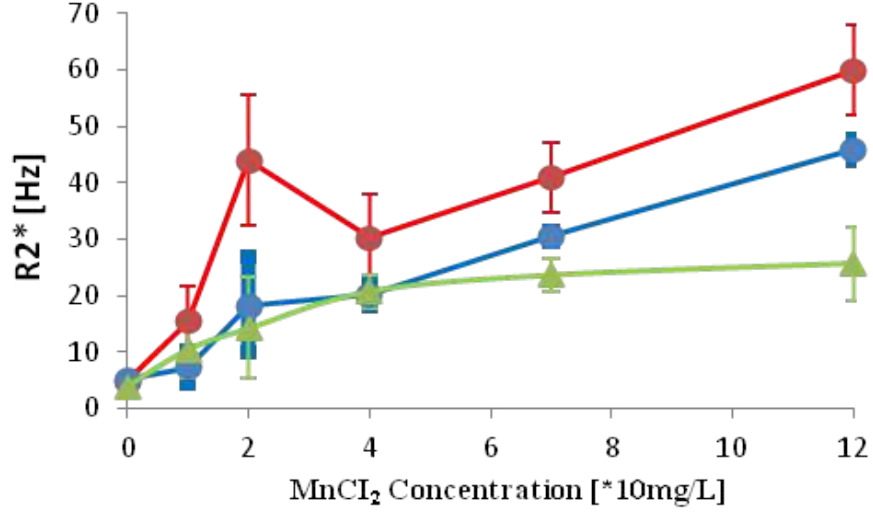


FIGURE 6: $R2^*$ value [Hz] as function of $MnCl_2$ concentrations [mg/L] within the phantom spheres, before (red line) and after correction with both LSC (green line) and NLSC (blue line)

Fig. 6 shows that at low $MnCl_2$ concentrations, both corrections remove the expected $R2^*$ bias; however near the right edge (sphere 2) and With increasing $MnCl_2$ concentrations (sphere 4 and 5), the LSC over corrects and the linear relationship of $R2^*$ with $MnCl_2$ is only preserved with the NLSC. The result clearly shows that the NLSC recover better the linear relationship between the $R2^*$ and $MnCl_2$ concentrations comparing to LSC, especially in regions suffering from huge field gradient inhomogeneities.

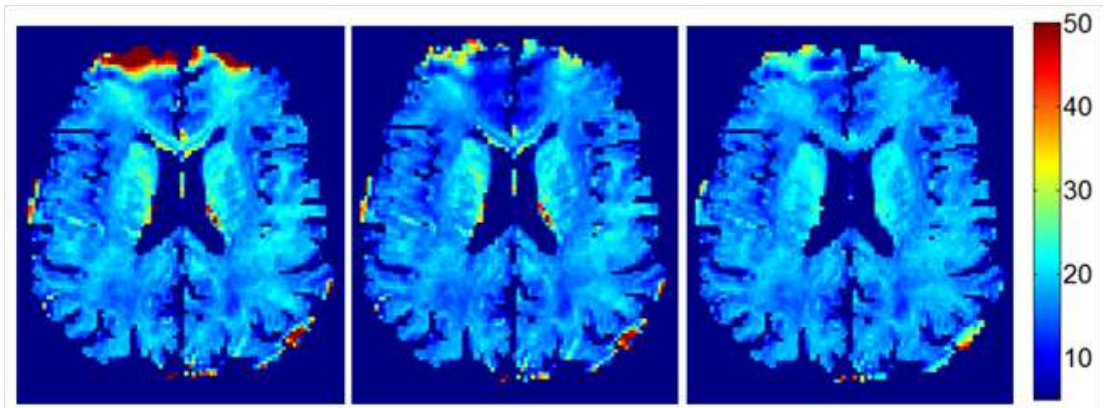


FIGURE 7: In-vivo DATA obtained from a human subject. Left image : $R2^*$ map without correction. Middle and right image present $R2^*$ corrected with LSC and NLSC respectively.

As in the phantom study, the presence of large macroscopic field gradient inhomogeneities in specific regions like the paranasal sinus, around the cingulate and near the brain edges ($SNR < 5$), leads to magnitude signal distortion and loss, therefore a huge $R2^*$ values over-estimation occurs Fig. 7 . In the center of the brain ($SNR > 20$), the field inhomogeneities are less significant and both LSC and NLSC provide approximately the same correction. In addition, we can remark an appearance of a spherical volume near the sinus region which has the same $R2^*$ value as the MS lesions in the same DATA. In Fig. 8, we can notice that without field inhomogeneities correction, the quantitative $R2^*$ parameters are over-estimated. After correction, the NLSC recovers the $R2^*$ values with high accuracy and less noise comparing to LSC method which tends to under-estimate the $R2^*$. NLSC methods remove the over-estimation and bring the $R2^*$ values into the rang of Ideal $R2^*$ even in the presence of high gradient variations.

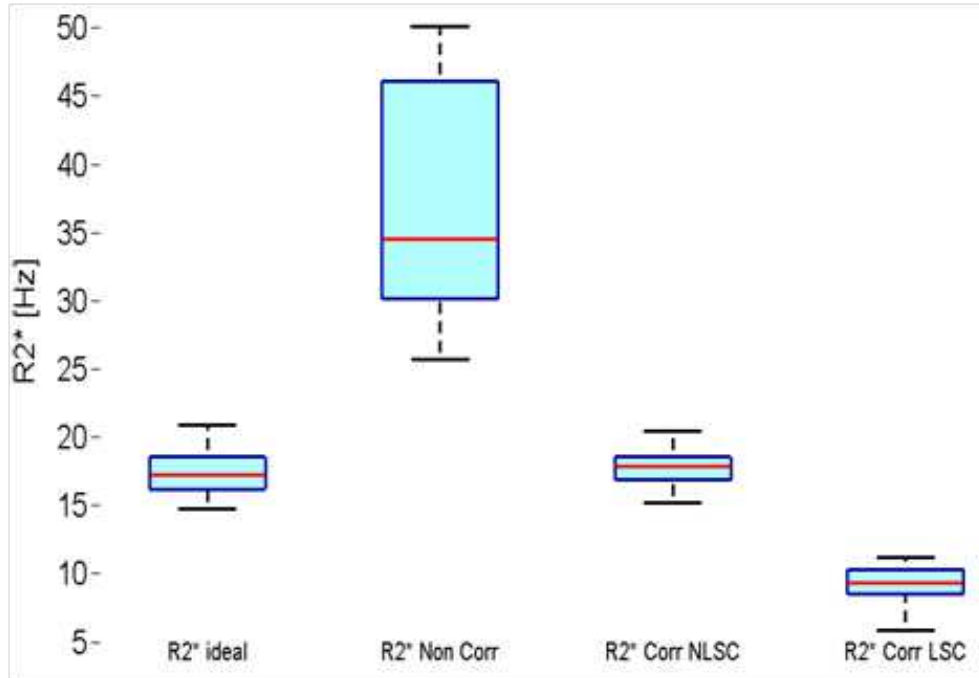


FIGURE 8: Boxplot of $R2^*$ values for 14 in-vivo DATA. VOI drawn in the paranasal sinus region where the field gradient is large ($> 50Hz/cm$) after correction with LSC and NLSC and compared with the $R2^*$ values of VOI drawn in the center of the brain where the field inhomogeneities are small (artifact free or Ideal $R2^*$) .

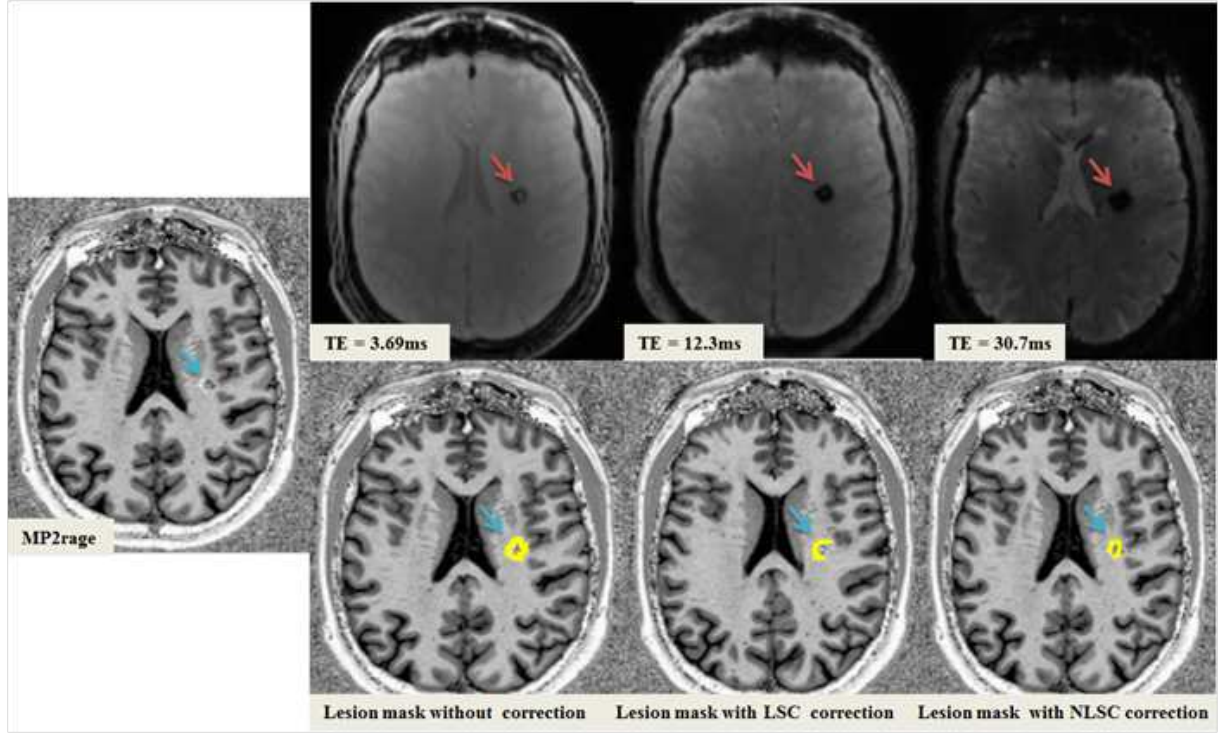


FIGURE 9: Left : MP2rage image with iron deposit lesion (blue arrow). Upper row : GRE images in different echo times showing the increasing blooming artifact around the iron deposit lesion (red arrows). Lower row : overlapped lesion mask which computed from the non-corrected and corrected $R2^*$ maps with LSC and NLSC.

Fig. 9, the upper row shows that the field distortion induced by the iron deposit creates a blooming artifact which increases with the echo time and may influence the lesion size measurement. In the MP2rage image(left), the lesion (blue arrow) appears small and well delineated and without any blooming artifacts, because MP2rage is less sensitive to the macroscopic B_0 field [1]. The $R2^*$ values in paranasal sinus region is highly over-estimated without applying correction, consequently the detection of any abnormal signal (high $R2^*$) is difficult. After correction with LSC and NLSC, the over-estimation is removed and the region appears free from any iron deposit. Also the size of the lesion is in concordance with size seen in MP2rage image. To well assess the lesion volume, we manually delineated the iron deposit lesion and computed the lesion volume from the MP2rage, non-corrected and corrected $R2^*$ maps with NLSC and LSC, the results are shown in the Fig. 10 .

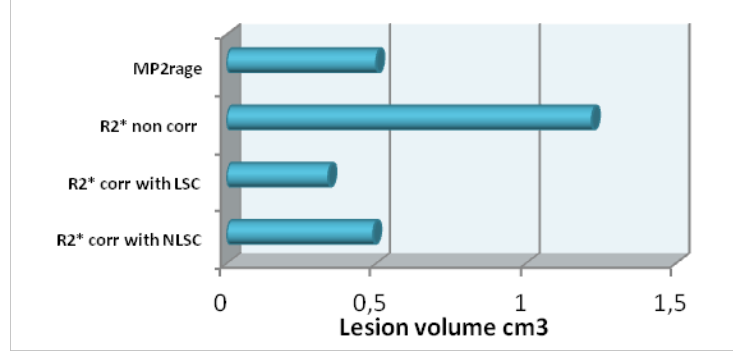


FIGURE 10: lesion volume computed from MP2rage, non-corrected and corrected $R2^*$ images with LSC and NLSC.

Fig. 10, the volume of the iron deposit lesion is over-estimated if we consider only the non-corrected $R2^*$ maps ($1.2 \pm 0.01 \text{ cm}^3$) comparing to the MP2rage volume ($0.5 \pm 0.01 \text{ cm}^3$). This result is not surprising because of the blooming artifact generated by the field distortion around the iron deposit lesion. With the NLSC correction, the computed volume ($0.49 \pm 0.01 \text{ cm}^3$) is approximately equal to the volume computed from the MP2rage comparing to the lesion volume with LSC ($0.34 \pm 0.1 \text{ cm}^3$); it means that both LSC and NLSC correction removes the macroscopic field inhomogeneities while keeping the microscopic information unchanged (iron deposit), but the over-estimation of the field distortion when the LSC is applied, may lead to small but not negligible underestimation of the lesion size. However, the result presented in this section remain subjective and dependent on the lesion delineation methods as well as the used statistics. Nevertheless, This application field of $R2^*$ correction will be further investigated in the detection of the microbleeds and validation of the cut-off point assumption to distinguish between the macro and microbleeds in patients with intracerebral hemorrhage.

The gradient computation near the brain edges is described as limitation for the $R2^*$ correction; existing solutions based on field map extrapolation beyond the air/tissue interfaces [2] or computing the gradient for the left-sided neighbor [4] have been demonstrated to improve the field characterization, but may still lead to inaccurate field estimates and are computationally expensive. However introducing the weighting factor $\psi(TEN)$ [eq.17] removes the gradient over-estimation while correcting the $R2^*$ maps without time consuming. The approximations used to build the algorithm like the ideal slice profile and the linear field variation across the image voxel are valid in isotropic high resolution imaging; extra field behavior measurements showed that no benefit from increasing polynomial fit order or voxel neighbors size while using high resolution images; in the case of low resolution images, the analytical Sinc solution changes But the nonlinear phase behavior remains valid and the phase dispersion can be computed using the proposed approach. The technique of combining the nonlinear phase behavior as function of echo time and the nonlinear field gradient evolution across the image voxel will be investigated in the future

for low resolution imaging. NLSC postprocessing correction procedure remains the fastest method, comparing to the iterative sinc correction in [5] which takes 134 hours for 3D image of 136x136x112 voxel, and the optimized Sinc correction in [22] which take 1 hours, the NLSC need only 2 minutes .

6 conclusion

Many studies have been dedicated to solve the problem of $R2^*$ correction from the macroscopic field inhomogeneties, but the complexity of the problem leaves it an open area for improvement. In this article we proposed a new approach to correct the quantitative $R2^*$ which we consider like a step in this direction. Conventionally, the existent algorithms assume the phase evolves linearly with time ; however, in the presence of a large B_{0macro} , e.g. near the edge of the brain, this assumption is broken and the phase evolution appears random and noisy. In this work, we hypothesized that the phase evolution in the presence of large B_{0macro} can be modeled and corrected using Gaussian-random-walk theory to compute the expected phase dispersion as function of echo time. So we reconsidered the basic theory and developed the NLSC method to correct from the field inhomogeneities whatever its severity. NLSC provided an equivalent correction as the LSC in region with high signal to noise ratio ($SNR > 20$) but appears more robust in regions of large or abrupt changes in B_{0macro} ($SNR < 5$). This correction technique shows promise to improve $R2^*$ measurements in regions of large susceptibilities and those applications need to be further investigated.

7 Acknowledgments

The author would like to thank Kieran O'brien and the Siemens team for the interesting discussions.

Références

- [1] Jose P. Marques and Tobias Kober, Gunnar Krueger, Wietske van der Zwaag, Pierre-François Van de Moortele, and Rolf Gruetter. A self-bias-field corrected sequence for improved segmentation and T1-mapping at high-field. *NeuroImage*, 49 :1271 :1281, 2010.
- [2] Grandin CB. Assessment of brain perfusion with MRI : methodology and application to acute stroke. *Neuroradiology*, 45 :755 :756, 2003.
- [3] Hernando D, Vigen KK, Shimakawa A, , and Reeder SB. r^2^* mapping in the presence of macroscopic B0 field variations. *Magn Reson Med*, 68 :830 :840, 2012.
- [4] Yablonskiy DA. Quantitation of intrinsic magnetic susceptibility-related effects in a tissue matrix : phantom study. *Magn Reson Med*, 39 :417 :428, 1998.
- [5] Anderson LJ and Holden S and Davis BA and Prescott E and Charrier CC and Bunce NH and Firmin DN and Wonke B and Porter J and Walker JM and Pennell DJ. Cardiovascular T2* (T2*) magnetic resonance for the early diagnosis of myocardial iron overload. *Eur Heart J*, 22 :2171 :179, 2001.
- [6] Haacke EM, Cheng NY, House MJ and Liu Q, Neelavalli J and Ogg RJ, and Khan A and Ayaz M and Kirsch W and Obenaus A. Imaging iron stores in the brain using magnetic resonance imaging. *Magn Reson Med*, 23 :000 :00, 2005.
- [7] Timothy G, St Pierre, Paul R Clark, Wanida Chua-anusorn, Adam J Fleming, Gary P. Jeffrey, John K. Olynik, Pensri Pootrakul, Erin Robins, and Robert Lindeman. Non-invasive measurement and imaging of liver iron concentrations using proton magnetic resonance. *Blood*, 105 :855 :861, 2005.
- [8] M Greenberg, Meike W Vernooij, Charlotte Cordonnier, Anand Viswanathan, Rustam Al-Shahi Salman, Steven Warach, Lenore J Launer, Mark A Van Buchem, and Monique M B Breteler ; for the Microbleed Study Group. Cerebral microbleeds : a guide to detection and interpretation. *IEEE Transactions on Image Processing*, 8, 2009.
- [9] An H and Lin W. Impact of intravascular signal on quantitative measures of cerebral oxygen extraction and blood volume under normo- and hypercapnic conditions using an asymmetric spin echo approach. *Magn Reson Med*, 50 :708 :716, 2003.
- [10] Dahnke H and Schaeffter T. Limits of detection of SPION at 3.0 T using T2 relaxometry. *Magn Reson Med*, 53 :1202 :1206, 2005.
- [11] G.E. Hagberg, I. Indovina, J.N. Sanes, and S. Posse. Real-time quantification of T2* changes using multi-echo planar imaging and numerical methods. *Magn Reson Med*, 48 :877 :882, 2002.
- [12] Pablo Irarrazabal, Craig H. Meyer, Dwight G. Nishirnura, and Albert Macovski. Inhomogeneity correction using an estimated linear field map. *Magn Reson Med*, 35 :278 :282, 1996.
- [13] Frahm J, Merboldt KD, and Hanack W. Direct FLASH MR imaging of magnetic field inhomogeneities by gradient compensation. *Magn Reson Med*, 0 :474 :480, 1988.

- [14] Gati JS, Menon RS, Ugurbil K, , and Rutt BK. Experimental determination of the bold eld strength dependence in vessels and tissue. *Neuroradiology*, 38 :296 :302, 1997.
- [15] Charles kittel. Solid state physics. 8th edition, 2005.
- [16] K. Kolliaa, S. Maderwalda, N. Putzkib, M. Schlamanna, J.M. Theysohna, O. Kraffa andc, M.E. Ladda andc, M. Forstinga, and I. Wankea. First clinical study on ultra-high-field mr imaging in patients with multiple sclerosis : Comparison of 1.5t and 7t. *AJNR Am J Neuroradiol*, 30 :699 :702, 209.
- [17] Fernandez Seara MA and Wehrli FW. Postprocessing technique to correct for background gradients in image-based $r2^*$ measurements. *magn Reson Med*, 44 :358 :66, 2000.
- [18] Wirestam R, Thilmann O, Knutsson L, Bjorkman-Burtscher IM, Larsson EM, and Stahlberg F. Comparison of quantitative dynamic susceptibility-contrast mri perfusion estimates obtained using different contrast-agent administration schemes at 3t. *Eur J Radiol. In press*, 00 :000 :000, 0000.
- [19] Baudrexel S, Volz S, Preibisch C, Klien JC, Steinmetz H, Hilker R, and Deichmann R. Rapid songle scan $t2^*$ ampping using exponential excitation pulses and image?ased correction for linear background gradient. *magn Reson Med*, 62 :263 :268, 2009.
- [20] Sammet S, Schmalbrock P, , and Knopp MV. Postprocessing correction for distortions in $t2^*$ decay caused by quadratic cross slice $b0$ inhomogeneity. *Magn Reson Med*, 63 :1258 :1268, 2010.
- [21] Fraank Spitzer. Principles of random walk . 2nd edition, 2001.
- [22] Wood JCand Enriquez Cand Ghugre Nand Tyzka JMand Carson Sand Nelson MDand Coates TD. Mri $r2$ and $r2^*$ mapping accurately estimates hepatic iron concentration in transfusion-dependent thalassemia and sickle cell disease patients. *Blood*, 106 :1460 :465, 2005.
- [23] van der Zwaag W, Francis S, Head K, Peters A, Gowland Pand Morris P, and Bowtell R. fmri at 1.5, 3 and 7 t : characterising bold signal changes. *Neuroimage*, 47 :1425 :434, 2009.
- [24] Z. Wang, A. C. Bovik, H. R. Sheikh, , and E. P. Simoncelli. Image quality assessment : From error visibility to structural similarity. *IEEE Transactios on Image Processing*, 13 :600 :612, 2004.
- [25] Yang X, Sammet S, Schmalbrock P, and Knopp MV. Postprocessing correction for distortions in $t2^*$ decay caused by quadratic cross-slic $b0$ inhomogeneity. *magn Reson Med*, 63 :1258 :268, 2010.
- [26] A Yablonskiy, Alexander I, Sukstanskii, Jie luo, and Xiaoqi Wang. Voxel spread functon method for correction of magnetic field inhomogeneity effects in quantitative gradient echo based mri. *magn Reson Med*, 00 :000 :000, 2012.
- [27] Huaiaren Zeng and R Todd Constable. Image distortion correction in epi : Comparison of field mapping with point spread function maping. *magn Reson Med*, 48 :137 :146, 2002.